

Quasiparticle dynamics and spin-orbital texture of the SrTiO₃ two-dimensional electron gas

P. D. C. King,^{1,2,*} S. McKeown Walker,³ A. Tamai,³ A. de la Torre,³ T. Eknapakul,⁴ P. Buaphet,⁴ S.-K. Mo,⁵ W. Meevasana,⁴ M. S. Bahramy,^{6,7} and F. Baumberger^{3,8,2,†}

¹*Kavli Institute at Cornell for Nanoscale Science, Ithaca, New York 14853, USA*

²*SUPA, School of Physics and Astronomy, University of St. Andrews, St. Andrews, Fife KY16 9SS, United Kingdom*

³*Département de Physique de la Matière Condensée, Université de Genève, 24 Quai Ernest-Ansermet, 1211 Genève 4, Switzerland*

⁴*School of Physics and NANOTEC-SUT Center of Excellence on Advanced Functional Nanomaterials, Suranaree University of Technology, Nakhon Ratchasima 30000, Thailand*

⁵*Advanced Light Source, Lawrence Berkeley National Lab, Berkeley, CA 94720, USA*

⁶*Quantum-Phase Electronics Center and Department of Applied Physics, The University of Tokyo, Tokyo 113-8656, Japan*

⁷*RIKEN center for Emergent Matter Science (CEMS), Wako 351-0198, Japan*

⁸*Swiss Light Source, Paul Scherrer Institut, CH-5232 Villigen PSI, Switzerland*

(Dated: May 11, 2022)

Two-dimensional electron gases (2DEGs) in SrTiO₃ have become model systems for engineering emergent behaviour in complex transition metal oxides. Understanding the collective interactions that enable this, however, has thus far proved elusive. We utilize angle-resolved photoemission to directly image the quasiparticle dynamics of the *d*-electron subband ladder of this complex-oxide 2DEG. Combined with realistic tight-binding supercell calculations, we uncover how quantum confinement and inversion symmetry breaking collectively tune the delicate interplay of charge, spin, orbital, and lattice degrees of freedom in this system. We demonstrate how they lead to pronounced orbital ordering, mediate an orbitally-enhanced Rashba splitting with complex subband-dependent spin textures and markedly change the character of electron-phonon coupling, co-operatively shaping the low-energy electronic structure of the 2DEG. Our results allow for a unified understanding of spectroscopic and transport measurements across different classes of SrTiO₃-based 2DEGs, and yield new microscopic insights on their functional properties.

PACS numbers:

The varied bulk properties of the ubiquitous perovskite oxide SrTiO₃, including quantum paraelectricity, dilute doping-induced superconductivity and high thermoelectric coefficients, reflect a subtle competition between interactions of the underlying quantum many-body system. Excitingly, a wealth of thermodynamic and transport measurements^{1–4} show that the balance of these interactions can be tuned to engineer striking new emergent properties when quantum confinement and doping are combined to create a two-dimensional electron gas (2DEG).^{5,6} This can be achieved by interfacing SrTiO₃ to other band or Mott insulators^{7–10}, can be formed at the free surface^{11–13}, or can be created in SrTiO₃-based transistors¹⁴.

Figure 1 summarises the resulting universal electronic structure, as revealed by angle-resolved photoemission (ARPES, see methods) from a SrTiO₃ surface 2DEG. Consistent with previous reports from both surface and interface 2DEGs,^{11–13,15,16} we find a broad bandwidth that extends up to ≈ 250 meV below the Fermi level. Here, we can resolve a ladder of at least three light sub-

band states that contribute concentric circular Fermi surface sheets, co-existing with just a single heavy electron band ($m^* = 14 \pm 3m_e$) that has a much shallower binding energy below 50 meV and gives rise to elliptical Fermi surfaces oriented along $\langle 10 \rangle$. From this Fermi surface topology together with the polarization dependence of our measured intensities (Supplementary Fig. S2), we assign not only the lowest¹², but rather the whole ladder of observed light states as having dominantly d_{xy} orbital character, while the heavy states derive from $d_{xz/yz}$ orbitals. This immediately indicates a strong breaking of the t_{2g} orbital degeneracy that is present in the bulk electronic structure of SrTiO₃¹⁷, driving a pronounced orbital ordering with a polarization $P = \frac{n(d_{xy}) - n(d_{xz/yz})}{n(d_{xy}) + n(d_{xz/yz})}$, which exceeds 30%, a lower limit directly derived from our experimentally-resolved Fermi surface areas.

This is a direct consequence of the real-space anisotropy of the orbital wavefunctions combined with inversion symmetry breaking by the electrostatic potential that defines the 2DEG, creating a steep asymmetric quantum well along the z -direction (Fig. 1(c)). As

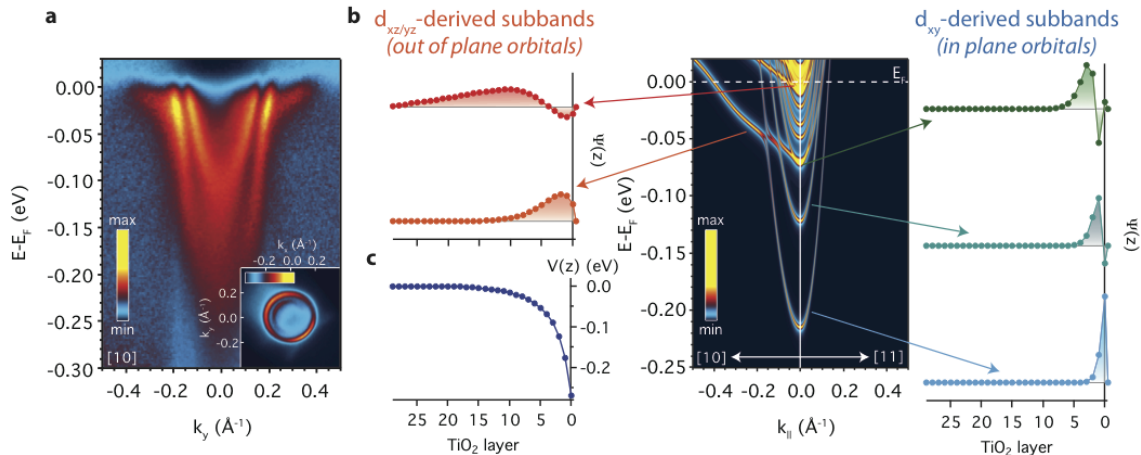


FIG. 1: **Orbital ordering of a two-dimensional electron gas (2DEG) in SrTiO₃.** (a) E vs. k dispersion from ARPES ($h\nu = 50$ eV, measured along the [10] direction), revealing a multi-orbital subband structure comprising co-existing ladders of light and massive d -electron subband states. The respective circular and faint elliptical Fermi surface pockets (measured with $h\nu = 51$ eV and the polarization along [11]) are shown in the inset. For the dispersion plot, a normalisation (division by the average MDC) has been applied to better reveal the massive band, as shown in Supplementary Fig. S1. (b) This electronic structure is well described by a self-consistent tight-binding supercell calculation. The spatial dependence of the subband wavefunctions along the confinement direction, $\Psi(z)$, reveal a pronounced real-space orbital ordering, a direct consequence of near-surface band bending (c).

shown by our self-consistent tight-binding supercell calculations (Fig. 1(b), see Methods), the resulting quantized subbands that derive from planar d_{xy} orbitals have wavefunctions reminiscent of the envelope functions of a semiconductor quantum well, except that in SrTiO₃ they are much more localized in real space, almost to within a single unit cell for the lowest subband state. In contrast, the potential variation acts as a much weaker perturbation on the out-of-plane $d_{xz/yz}$ orbitals, which have much larger hopping amplitudes along the z -direction. The resulting subbands sit close to the top of the potential well, ensuring wavefunctions that penetrate much deeper into the bulk. This disparate spatial extent of the subband states is consistent with their relative spectral weight in our surface-sensitive ARPES measurements.

The same breaking of inversion symmetry that drives this orbital ordering can additionally lift the spin degeneracy through a Bychkov-Rashba-type spin-orbit interaction¹⁸ (Fig. 2). Focussing near the band bottom of the lowest d_{xy} band, we indeed find a small characteristic splitting between the calculated energy of spin-up and spin-down states, $\delta E = 2\alpha k_{\parallel}$, with a Rashba parameter, $\alpha = 0.003$ eVÅ. The non-negligible splitting found here, despite the modest spin-orbit interaction in 3d transition metals, is indicative of the very strong electric field gradient of the confining potential which exceeds 2×10^8 Vm⁻¹ within the first 2 unit cells where the lowest subband state is confined. For the more delo-

calized second d_{xy} subband, whose wavefunction extends into regions of shallower band bending, we find a slightly smaller Rashba parameter $\alpha = 0.0014$ eVÅ, confirming that the strength of the spin splitting is controlled by the confining electric field. This should therefore be directly tuneable by electrical gating, suggesting a potential route towards spintronic control in oxides.

Unlike typical Rashba systems such as the Au(111) surface, however, here the interplay between orbital ordering and spin-orbit interactions leads to an exotic spin texture of the 2DEG states. While the approximately perpendicular spin-momentum locking ensures tangential spin winding around the circular d_{xy} sections of Fermi surface, it leads to spins aligned almost perpendicular to the Fermi surface for large sections of the extremely anisotropic d_{xz} (d_{yz}) sheets. Intriguingly, around the crossings of d_{xy} and $d_{xz/yz}$ states, the spins of neighbouring Fermi surfaces align (anti-)parallel with a $|\downarrow\rangle|\uparrow\rangle|\uparrow\rangle|\downarrow\rangle$ ordering, reflecting a dominance of *interband* spin-orbit interactions in this system. This causes the direction of spin winding of the outer d_{xy} -derived Fermi surfaces to abruptly switch sign across the hybridization gaps (Fig. 2(c)), and leads to strongly canted spin textures, moving from tangential to radial, for several inner Fermi surfaces whose orbital character evolves from d_{xy} - to $d_{xz/yz}$ -like around the Fermi surface (Supplemental Fig. S3).

Moreover, the $|\downarrow\rangle|\uparrow\rangle|\uparrow\rangle|\downarrow\rangle$ alignment ensures maximum

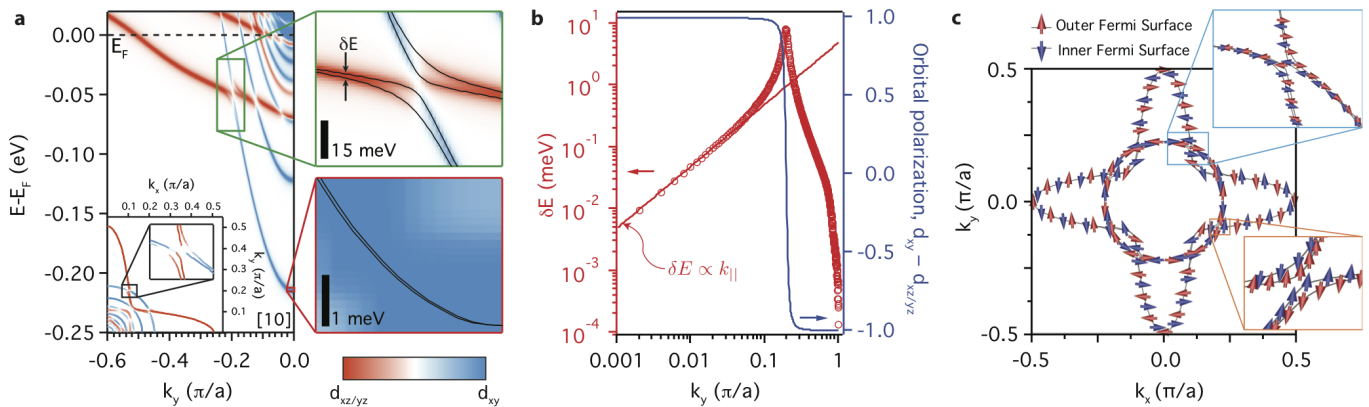


FIG. 2: **Orbitaly-enhanced Rashba spin splitting.** (a) Orbitaly-resolved electronic structure of the 2DEG along the [10] direction and around the Fermi surface (inset). Magnified views reveal a weak Rashba-type spin splitting around the band bottom, which becomes significantly enhanced at the crossings of the light and heavy subband states where the orbital character becomes strongly mixed. The splitting and orbital character are quantified in (b) for the lowest subbands. (c) Spin angular momenta of the outer (red) and inner (blue) spin-split branches of the largest Fermi surface sheets, showing an unconventional spin texture arising from the combination of Rashba interactions and orbital ordering. The spin texture of the full Fermi surface is shown in Supplemental Figure S3.

possible hybridization gaps are opened. Indeed, we find that the orbital character becomes strongly mixed and the spin splitting increases by approximately an order of magnitude close to such crossings of light d_{xy} and heavy $d_{xz/yz}$ subbands.¹⁹ Our layer-projected calculations indicate that the subband wavefunctions become more delocalized in the z -direction close to these band crossings, a natural consequence of the stronger overlap of neighbouring $d_{xz/yz}$ orbitals along z (Supplementary Fig. S4). This delocalization would naively be expected to reduce the strength of the Rashba effect. In contrast, its significant enhancement here points to a dominant role of inter-orbital hopping in stabilizing surprisingly-large spin splittings.

This provides a microscopic origin for the pronounced spin splittings inferred from magnetotransport,^{22–24} despite the small atomic spin-orbit interaction of SrTiO₃. It further rationalises the increased splitting reported when the heavy $d_{xz/yz}$ subbands become populated in electrically-gated SrTiO₃/LaAlO₃ interface 2DEGs.²⁵ Moreover, the crossover from k -linear to strongly enhanced spin splitting that we find here readily explains the approximately k^3 dependence of the splitting reported in recent transport measurements.²⁶ It is, however, quite distinct from the functional form of conventional Rashba splitting, providing strong constraints for its influence on magnetism²⁷ and superconductivity,²⁸ and revealing a particularly delicate interplay between spin and orbital degrees of freedom in SrTiO₃-based 2DEGs.

In Figure 3, we further uncover a pronounced role of electron-phonon interactions on this rich hierarchy of electronic states. Unlike in bulk-doped SrTiO₃, where

the Fermi energy is typically only a few meV and the electron-phonon interaction is thus non-retarded, the occupied widths of different subbands of the 2DEG range from almost zero up to values greater than the highest phonon frequency of ≈ 100 meV. This is an unusual situation, neither described by the adiabatic ($\hbar\omega_D \ll E_F$) nor the anti-adiabatic ($\hbar\omega_D \gg E_F$) approximation, and points to a complex influence of electron-phonon coupling in this system. We extract the corresponding self-energy, $\Sigma_{e-ph}(\omega) = \Sigma'(\omega) + i\Sigma''(\omega)$, from our ARPES measurements of the lowest subband along the [11] direction (see methods), where we resolve an isolated band all the way up to E_F . The slope of Σ' at the Fermi level yields an electron-phonon coupling strength of $\lambda = 0.7(1)$, while its broad maximum between $\approx 20 - 60$ meV is indicative of coupling to multiple modes. Indeed, the experimentally-determined self-energy is in excellent agreement with a calculation within Eliashberg theory that assumes a coupling function $\alpha^2F(\omega)$ proportional to the entire phonon density of states associated with the motion of oxygen and Ti ions³⁰ and includes the realistic 2DEG electron density of states from our tight-binding calculation.

Together with a moderate correlation-induced mass enhancement of ≈ 1.4 that we estimate from a Kramers-Kronig transform of a Fermi-liquid contribution to the imaginary part of the self-energy, our analysis suggests an overall mass enhancement arising from many-body interactions of $m^*/m_{\text{band}} \approx 2.1$, close to the values deduced for lightly-doped bulk SrTiO₃ from measurements of the electronic specific heat³¹ and optical spectroscopy³². The nature of the electron-phonon coupling, however, is very different. In lightly-doped bulk SrTiO₃, it is dominated by the long-range coupling to longitudi-

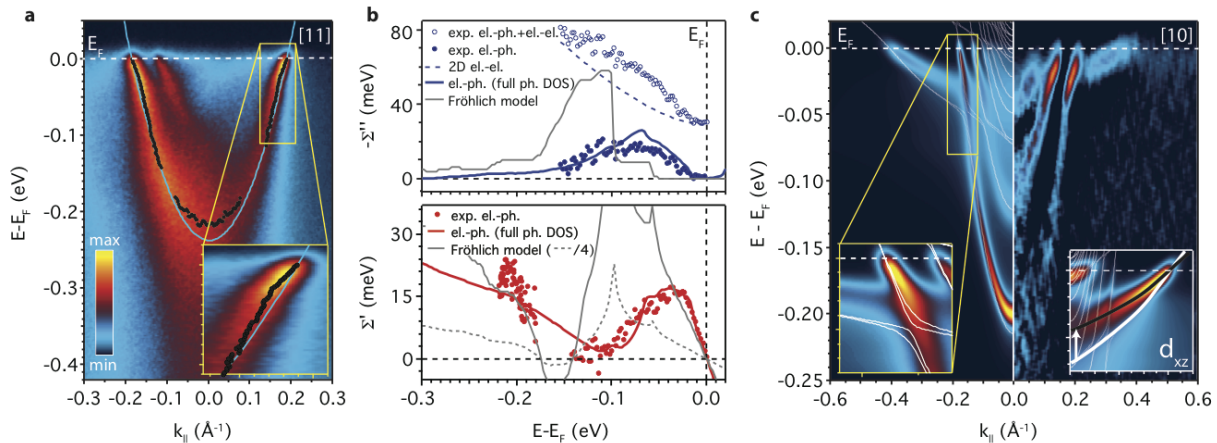


FIG. 3: **Quasiparticle dynamics of the subband states.** (a) ARPES measurements along the [11] direction ($h\nu = 51$ eV), together with the peak positions of fits to MDCs and EDCs (black dots) and a cosine ‘bare band’ dispersion (blue line). The data reveal pronounced signatures of electron-phonon coupling. Particularly apparent is a low-energy kink in the dispersion at $\omega \approx 30$ meV, shown magnified inset. (b) Real, Σ' , and imaginary, Σ'' , parts of the extracted self-energy. The open blue symbols show Σ'' before subtraction of an electron-electron scattering contribution to the total measured imaginary part of the self-energy, approximated here by the expression $\Sigma''_{e-e}(\omega) = \beta\omega^2[1 + 0.53 \ln(\omega/E_F)]$ for a 2D Fermi liquid (dashed line, $\beta = 1.5$ eV $^{-1}$, $E_F = 0.25$ eV). The solid lines are calculated electron-phonon self energies with the Eliashberg function proportional to the full phonon density of states (red/blue) or for coupling to three longitudinal optical phonons (black), which dominate the interaction in lightly doped bulk SrTiO $_3$. (c, left) Calculated electron-phonon spectral function, $A(k, \omega)$, along the [10] direction (see Methods). This reveals complete bandwidth renormalization of the heavy states (particularly apparent when $A(k, \omega)$ is projected only onto d_{xz} orbitals as shown in the right inset), and kinks in the light d_{xy} subband dispersions at their crossings with this renormalized heavy state (left inset), both in good agreement with our experimental measurements, shown in the right half using curvature analysis 29 of the raw data.

nal optical (LO) phonons as described by the Fröhlich model. 32,33 This model predicts much weaker coupling to low-energy modes than observed here, but a significantly stronger coupling to the highest LO phonon at 100 meV, as evident from a calculation employing coupling strengths from bulk SrTiO $_3$, 33,34 which yield an electron-phonon self-energy in clear contrast to our experimental findings (Fig. 3(b)).

This likely reflects a collapse of the dielectric constant driven by the electric field that confines the 2DEG, 11,35 as well as higher carrier densities compared to bulk SrTiO $_3$, leading to shorter electronic screening lengths. The enhanced coupling to low-energy phonons for the 2DEG leads to a pronounced kink in the dispersion of the d_{xy} subbands at an energy around 30 meV. We resolve these along both the [10] and [11] directions for the first two d_{xy} subbands. Crucially, the resulting enhanced quasiparticle mass, which we estimate as 1.1(2) m_e from our measured Fermi velocities, rectifies the discrepancy between the light masses around 0.6 m_e reported in earlier ARPES studies of SrTiO $_3$ surface 2DEGs 11,12 and recent quantum oscillation experiments that revealed effective masses typically around 1 m_e . 36,37

Intriguingly, along [10] the kink energy coincides almost exactly with the crossing of the light d_{xy} and heavy d_{xz} subband states. This behaviour is well captured

by our spectral function simulations calculated from our tight-binding bare dispersions and electron-phonon self-energy. These illustrate a very different effect of electron-phonon interactions on the heavy compared to the light subbands of the 2DEG, the former coupling to phonons with frequencies ranging from below to above the bare band width. Our calculations reveal that electron-phonon coupling essentially results in an overall bandwidth renormalisation of these states, in agreement with our experimental data where we find the band bottom of the heavy state substantially above the value predicted by our model tight binding calculations. This effectively pins the crossings of orbitally-ordered d_{xy} and $d_{xz/yz}$ subbands to the low-energy peak in the phonon density of states, which in turn sets the energy scale for the onset of orbitally-enhanced spin-splittings around these crossings. Our measurements therefore reveal a particularly delicate interplay between orbital ordering, electron-phonon coupling, and spin-orbit interactions governing the low-energy electronic structure of the SrTiO $_3$ 2DEG (Figure 4), with quantum size effects entangling the charge, spin, orbital, and lattice degrees of freedom on an energy scale ≤ 30 meV. This will dominate both the transport and thermodynamic properties of this emergent electronic system.

Methods

Angle-resolved photoemission: ARPES measurements were performed at the CASIOPEE beamline of SOLEIL

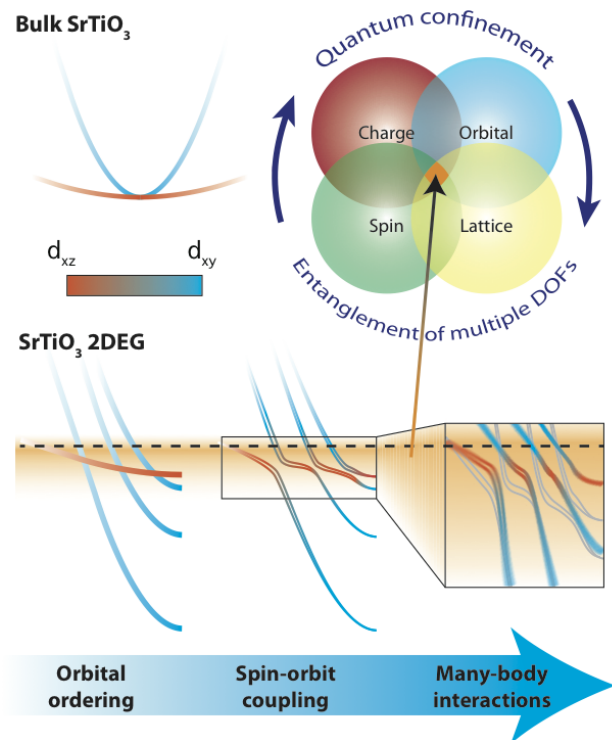


FIG. 4: **Hierarchy and interplay of charge, spin, orbital, and lattice degrees of freedom in the SrTiO₃ 2DEG.** In the formation of the 2DEG, quantum confinement reconstructs the bulk electronic structure into a rich array of intersecting orbitally-ordered subband states. The interplay of this with spin-orbit coupling lifts the spin degeneracy of these bands, particularly strong around their crossings, through an orbitally-enhanced Rashba-like interaction. Electron-phonon and electron-electron interactions further renormalise these spin-split dispersions, increasing the quasiparticle masses close to the Fermi level, and causing a complete bandwidth narrowing of the shallow $d_{xz/yz}$ states that pins the orbitally-ordered band crossings close to the energy of the lowest phonon mode. This, in turn, sets the energy scale for enhanced spin-orbit splittings around these crossings, strongly entangling the underlying degrees of freedom of the 2DEG on a low energy scale (orange shading).

synchrotron, the SIS beamline of the Swiss Light Source, and beamline 10.0.1 of the Advanced light source using Scienta R4000 hemispherical electron analysers, and with base pressures below 5×10^{-11} mbar. Single crystal SrTiO₃ commercial wafers were cleaved *in situ* at the measurement temperature of $T = 20 - 30$ K along notches defining a (100) plane. Measurements were performed on stoichiometric transparent insulating samples as well as very lightly La-doped samples (Sr_{1-x}La_xTiO₃ with $x = 0.001$) to help avoid charging. 2DEGs were induced at the bare surface by exposure to intense UV synchrotron light.¹¹ The samples were exposed to irradiation doses $\gtrsim 1000$ Jcm⁻² to saturate the formation of the 2DEG, and we experimentally confirmed that saturation was reached before starting any of the measurements presented here. The data shown here was measured using *s*-polarised photons of 51 or 55 eV, except

for the Fermi surface maps shown in the supplemental information that used 43 eV *s*- and *p*-polarised light. All measurements were performed in the second Brillouin zone.

Self-energy determination: To determine the electron-phonon self-energy experimentally, we fit momentum distribution curves (MDCs) and energy distribution curves (EDCs) of the lowest d_{xy} subband measured along the [11] direction. We chose this band as its dispersion does not intersect that of the heavy $d_{xz/yz}$ subbands up to the chemical potential along this direction (Fig. 1(b)), allowing us to perform a quantitative analysis over an extended energy range, free from complications associated with the hybridization of different subbands. The real part of the self-energy, $\Sigma'(\omega)$, is given by the difference between our extracted dispersion and that of a ‘bare’ band. In order to derive a Kramers-Kronig consistent self-energy, we take the cosine bare band shown in Fig. 3(a), which includes a moderate band width renormalization due to electron correlations. We extract the imaginary part of the self energy, $\Sigma''(\omega) = \Delta k(\omega)/2 \cdot \partial\epsilon/\partial k$, where Δk is the full width at half maximum of Lorentzian fits to MDCs, and $\partial\epsilon/\partial k$ is the bare band dispersion. This results in an imaginary part that includes a contribution from electron-electron interactions, which we approximate by the expression for a two-dimensional Fermi liquid $\Sigma''_{e-e}(\omega) = \beta\omega^2[1 + 0.53\ln(\omega/E_F)]$. Subtracting this contribution with realistic parameter values of $\beta = 1.5$ eV⁻¹ and $E_F = 0.25$ eV from our total extracted Σ'' (see Fig. 3(b)) yields the imaginary part of the electron-phonon self-energy.

Electronic structure and self-energy calculations: To calculate the subband structure, we start from a relativistic density functional theory (DFT) calculation of bulk SrTiO₃ using the modified Becke-Johnson exchange potential and Perdew-Burke-Ernzerhof correlation functional as implemented in the WIEN2K program³⁸. The muffin-tin radius of each atom R_{MT} was chosen such that its product with the maximum modulus of reciprocal vectors K_{max} become $R_{MT}K_{max} = 7.0$. The Brillouin zone was sampled by a $15 \times 15 \times 15$ k -mesh. We downfold this using maximally-localized Wannier functions to generate a set of bulk tight-binding transfer integrals, and then incorporate these into a 30 unit cell supercell with additional on-site potential terms to account for band bending via an electrostatic potential variation. We solve this self-consistently with Poisson’s equation, incorporating an electric field-dependent dielectric constant,³⁵ to yield the bare band dispersions including Rashba-type spin splitting of the 2DEG. We stress that the total magnitude of the band bending is the only adjustable parameter, and yields a realistic electronic structure in good agreement with our spectroscopic measurements apart from our observed signatures of electron-phonon interactions which are not included at the level of DFT. To incorporate these, we calculate the self-energy $\Sigma_{e-ph}(\omega)$ in an Eliashberg model,

$$\Sigma_{e-ph}(\omega) = \int_{-E_F}^{\infty} N(\epsilon) d\epsilon \int_0^{\tilde{\omega}_{max}} d\tilde{\omega} \alpha^2 F(\tilde{\omega}) \times \left\{ \frac{f(-\epsilon, T) + n(\tilde{\omega}, T)}{\omega - \epsilon - \tilde{\omega} + i\delta^{\pm}} + \frac{f(\epsilon, T) + n(\tilde{\omega}, T)}{\omega - \epsilon + \tilde{\omega} + i\delta^{\pm}} \right\}$$

where $N(\epsilon)$ is the bare electronic density of states determined from our tight binding calculations and $f(\epsilon, T)$ and $n(\tilde{\omega}, T)$

are the Fermi and Bose occupation factors. For the coupling function $\alpha^2 F(\tilde{\omega})$ we use two different models. The blue line in Fig. 3(b) assumes $\alpha^2 F(\tilde{\omega})$ proportional to the entire O- and Ti-derived phonon density of states from Ref.³⁰, while the black line is a calculation for the coupling strengths given in Refs.^{33,34} for the three longitudinal optical phonons that were found to dominate the electron-phonon interaction in lightly doped bulk samples. We then calculate the spectral function

$$A(k, \omega) = -\frac{1}{\pi} \frac{\Sigma''(\omega)}{[\omega - \epsilon(k) - \Sigma'(\omega)]^2 + [\Sigma''(\omega)]^2}$$

where the bare band dispersion $\epsilon(k)$ is taken from our tight-binding calculation. To better compare with our experimental data in Fig. 3(c), we project this onto different atomic orbitals, and include contributions from d_{xy} and d_{xz} but not d_{yz} orbitals to account for transition matrix elements in our experimental geometry. We additionally project the calculation onto different layers of our supercell, and incorporate an exponential attenuation of signal with depth below the surface in photoemission, assuming an inelastic mean free path of 5 Å, into our simulation. Finally, we convolve the simulated spectral function with a 2D Gaussian to account for an experimental energy and momentum resolution of 0.01 eV and 0.015 Å⁻¹, respectively.

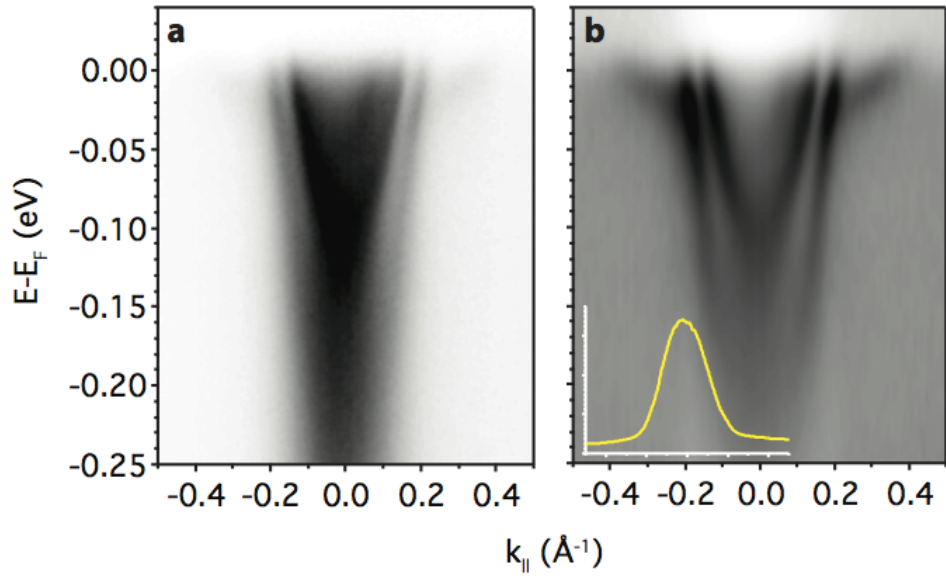
* Electronic address: philip.king@st-andrews.ac.uk

† Electronic address: Felix.Baumberger@unige.ch

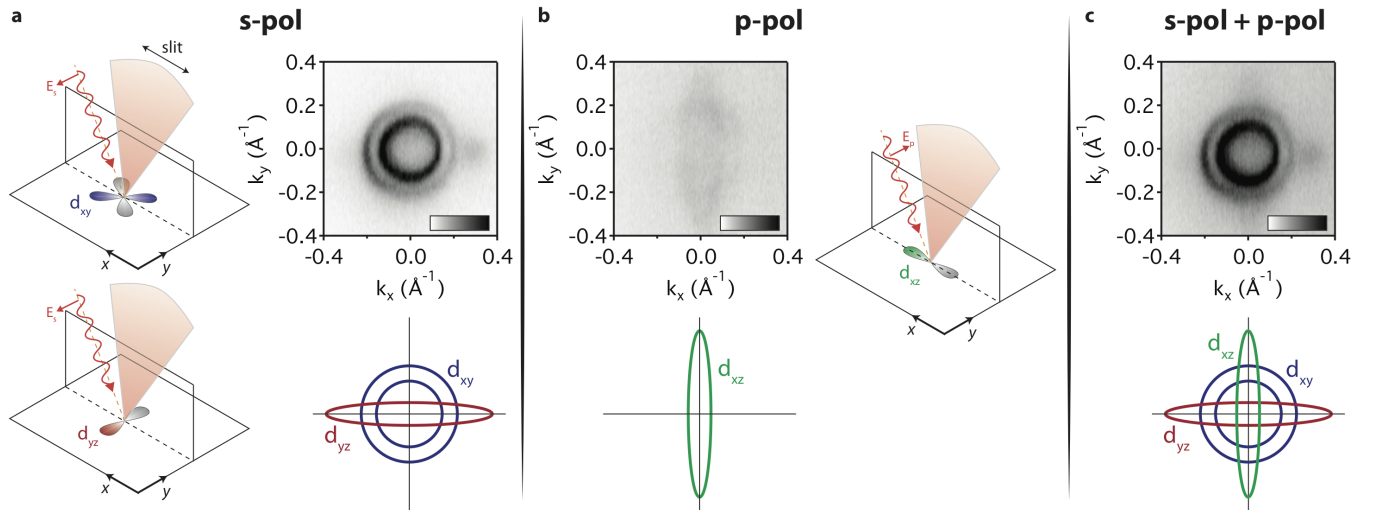
- [1] Reyren, N. *et al.* Superconducting Interfaces Between Insulating Oxides. *Science* **317**, 1196–1199 (2007).
- [2] Caviglia, A. D. *et al.* Electric field control of the LaAlO₃/SrTiO₃ interface ground state. *Nature* **456**, 624–627 (2008).
- [3] Bert, J. A. *et al.* Direct imaging of the coexistence of ferromagnetism and superconductivity at the LaAlO₃/SrTiO₃ interface. *Nature Phys.* **7**, 767–771 (2011).
- [4] Li, L., Richter, C., Mannhart, J. & Ashoori, R. C. Coexistence of magnetic order and two-dimensional superconductivity at LaAlO₃/SrTiO₃ interfaces. *Nature Phys.* **7**, 762–766 (2011).
- [5] Mannhart, J. & Schlom, D. G. Oxide Interfaces—An Opportunity for Electronics. *Science* **327**, 1607–1611 (2010).
- [6] Hwang, H. Y. *et al.* Emergent phenomena at oxide interfaces. *Nature Mater.* **11**, 103–113 (2012).
- [7] Ohtomo, A. & Hwang, H. Y. A high-mobility electron gas at the LaAlO₃/SrTiO₃ heterointerface. *Nature* **427**, 423–426 (2004).
- [8] Ohtomo *et al.*, A. Artificial charge modulation in atomic scale perovskite titanate superlattices. *Nature* **419**, 378 (2002).
- [9] Moetakef, P. *et al.* Electrostatic carrier doping of GdTiO₃/SrTiO₃ interfaces. *Appl. Phys. Lett.* **99**, 232116 (2011).
- [10] Choi, W. S., Lee, S., Cooper, V. R. & Lee, H. N. Fractionally δ -Doped Oxide Superlattices for Higher Carrier Mobilities. *Nano Lett.* **12**, 4590–4594 (2012).
- [11] Meevasana, W. *et al.* Creation and control of a two-dimensional electron liquid at the bare SrTiO₃ surface. *Nature Mater.* **10**, 114–118 (2011).
- [12] Santander-Syro, A. F. *et al.* Two-dimensional electron gas with universal subbands at the surface of SrTiO₃. *Nature* **469**, 189–193 (2011).
- [13] D’Angelo, M. *et al.* Hydrogen-Induced Surface Metalization of SrTiO₃(001). *Phys. Rev. Lett.* **108**, 116802 (2012).
- [14] Ueno, K. *et al.* Electric-field-induced superconductivity in an insulator. *Nature Mater.* **7**, 855–858 (2008).
- [15] Berner, G. *et al.* Direct k -Space Mapping of the Electronic Structure in an Oxide-Oxide Interface. *Phys. Rev. Lett.* **110**, 247601 (2013).
- [16] Plumb, N. C. *et al.* Mixed dimensionality of confined conducting electrons tied to ferroelectric surface distortion on an oxide. *arXiv:1302.0708* (2013).
- [17] Salluzzo, M. *et al.* Orbital Reconstruction and the Two-Dimensional Electron Gas at the LaAlO₃/SrTiO₃ Interface. *Phys. Rev. Lett.* **102**, 166804 (2009).
- [18] Bychkov, Y. A. & Rashba, E. I. Properties of a 2D electron gas with lifted spectral degeneracy. *JETP Lett.* **39**, 78 (1984).
- [19] After completing our calculations, we became aware of recent model calculations that observed similar enhancements of the spin splitting around band crossings.^{20,21} Here, we demonstrate that this is an inherent property of orbital hybridization and a dominance of inter-band spin-orbit interactions of the real multi-subband structure of a SrTiO₃ 2DEG, is a direct consequence of broken inversion symmetry driving both strong orbital ordering and pronounced Rashba-like interactions in this system, and show how these together lead to an unconventional spin texture of the resulting electronic system.
- [20] Zhong, Z., Tóth, A. & Held, K. Theory of spin-orbit coupling at LaAlO₃/SrTiO₃ interfaces and SrTiO₃ surfaces. *Phys. Rev. B* **87**, 161102 (2013).
- [21] Khalsa, G., Lee, B. & MacDonald, A. H. Theory of t_{2g} electron-gas Rashba interactions. *arXiv:1301.2784* (2013).
- [22] Caviglia, A. D. *et al.* Tunable Rashba Spin-Orbit Interaction at Oxide Interfaces. *Phys. Rev. Lett.* **104**, 126803 (2010).
- [23] Ben Shalom, M., Sachs, M., Rakhmilevitch, D., Palevski, A. & Dagan, Y. Tuning Spin-Orbit Coupling and Superconductivity at the SrTiO₃/LaAlO₃ Interface: A Magnetotransport Study. *Phys. Rev. Lett.* **104**, 126802 (2010).
- [24] Joshua, A., Pecker, S., Ruhman, J., Altman, E. & Ilani, S. A universal critical density underlying the physics of electrons at the LaAlO₃/SrTiO₃ interface. *Nature Commun.* **3**, 1129– (2012).
- [25] Fête, A., Gariglio, S., Caviglia, A. D., Triscone, J.-M. & Gabay, M. Rashba induced magnetoconductance oscillations in the LaAlO₃-SrTiO₃ heterostructure. *Phys. Rev. B* **86**, 201105 (2012).
- [26] Nakamura, H., Koga, T. & Kimura, T. Experimental Evidence of Cubic Rashba Effect in an Inversion-Symmetric Oxide. *Phys. Rev. Lett.* **108**, 206601 (2012).
- [27] Fischer, M. H., Raghu, S. & Kim, E.-A. Spin-orbit coupling in LaAlO₃/SrTiO₃ interfaces: magnetism and orbital ordering. *New J. Phys.* **15**, 023022 (2013).
- [28] Michaeli, K., Potter, A. C. & Lee, P. A. Superconducting and Ferromagnetic Phases in SrTiO₃/LaAlO₃ Oxide Interface Structures: Possibility of Finite Momentum Pair-

- ing. *Phys. Rev. Lett.* **108**, 117003 (2012).
- [29] Zhang, P. *et al.* A precise method for visualizing dispersive features in image plots. *Rev. Sci. Instrum.* **82**, 043712 (2011).
- [30] Choudhury, N., Walter, E. J., Kolesnikov, A. I. & Loong, C.-K. Large phonon band gap in SrTiO₃ and the vibrational signatures of ferroelectricity in ATiO₃ perovskites: First-principles lattice dynamics and inelastic neutron scattering. *Phys. Rev. B* **77**, 134111 (2008).
- [31] Ambler, E., Colwell, J. H., Hosler, W. R. & Schooley, J. F. Magnetization and Critical Fields of Superconducting SrTiO₃. *Phys. Rev.* **148**, 280–286 (1966).
- [32] van Mechelen, J. L. M. *et al.* Electron-Phonon Interaction and Charge Carrier Mass Enhancement in SrTiO₃. *Phys. Rev. Lett.* **100**, 226403 (2008).
- [33] Verbist, G., Peeters, F. M. & Devreese, J. T. Extended stability region for large bipolarons through interaction with multiple phonon branches. *Ferroelectrics* **130**, 27–34 (1992).
- [34] Meevasana, W. *et al.* Strong energy-momentum dispersion of phonon-dressed carriers in the lightly doped band insulator SrTiO₃. *New J. Phys.* **12**, 023004 (2010).
- [35] Copie, O. *et al.* Towards Two-Dimensional Metallic Behavior at LaAlO₃/SrTiO₃ Interfaces. *Phys. Rev. Lett.* **102**, 216804 (2009).
- [36] Caviglia, A. D. *et al.* Two-Dimensional Quantum Oscillations of the Conductance at LaAlO₃/SrTiO₃ Interfaces. *Phys. Rev. Lett.* **105**, 236802 (2010).
- [37] Kim, M. *et al.* Fermi Surface and Superconductivity in Low-Density High-Mobility δ -Doped SrTiO₃. *Phys. Rev. Lett.* **107**, 106801 (2011).
- [38] Blaha, P., Schwarz, K., Madsen, G., Kvasnicka, D. & Luitz, J. Wien2k package. available at <http://www.wien2k.at>.

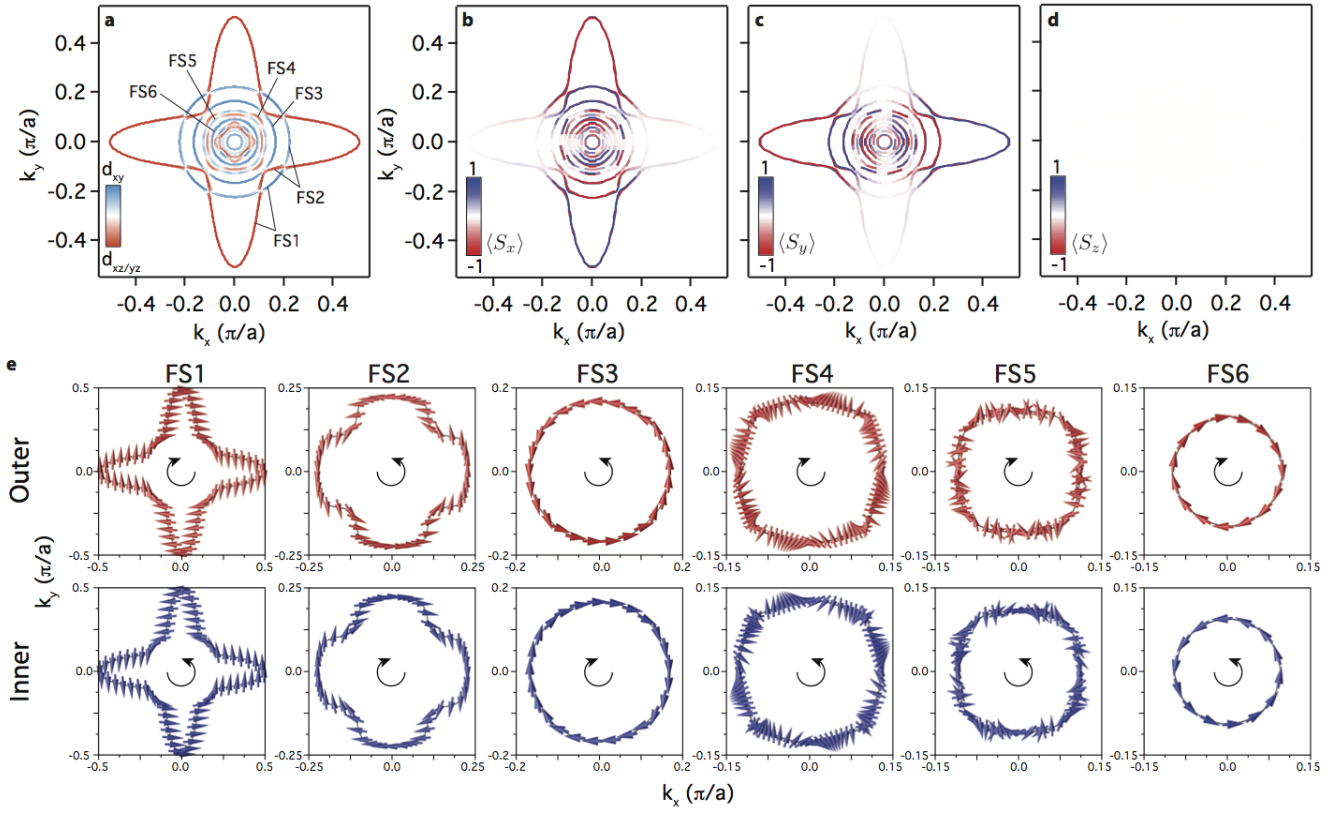
Acknowledgements This work was supported by the U.K. EPSRC, the ERC, the Scottish Funding Council, The Thailand Research Fund, Office of the Higher Education Commission, Suranaree University of Technology, and the Japan Society for the promotion of Science (JSPS), through the ‘Funding Program for World-Leading Innovative R&D on Science and Technology (FIRST Program)’, initiated by the council for Science and Technology policy (CSTP). We acknowledge SOLEIL (beamline CASSIOPEE), the ALS (beamline 10.0.1), and SLS (SIS beamline) for provision of synchrotron radiation facilities, and in particular N.C. Plumb, M. Radović, and M. Shi (SLS) and P. Le Fèvre, F. Bertran and A. Taleb-Ibrahimi (SOLEIL) for technical assistance. The Advanced Light Source is supported by the Director, Office of Science, Office of Basic Energy Sciences, of the U.S. Department of Energy under Contract No. DE-AC02-05CH11231. We gratefully acknowledge C. Bell, C. Berthod, V. Cooper, A. Fête, H.Y. Hwang, M. Kim, J. Mannhart, D. van der Marel, and J.-M. Triscone for useful discussions.



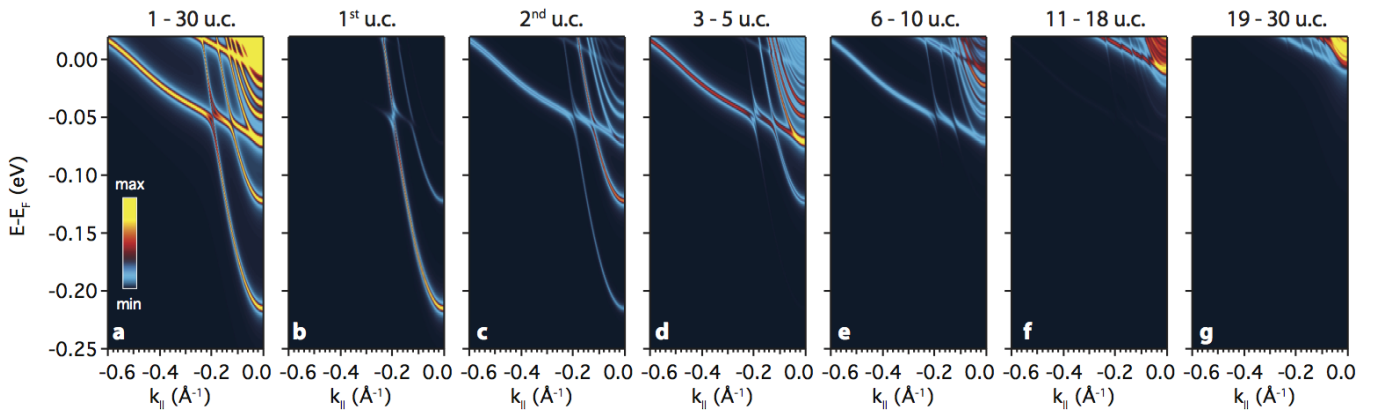
Supplementary Figure 1: (a) Raw data of the spectrum shown in Fig. 1a of the main manuscript, clearly revealing three light subband states as well as weak spectral weight from a single heavy band at lower binding energy. (b) This latter feature is strongly enhanced by dividing by the average MDC intensity (shown inset).



Supplementary Figure 2: Fermi surface of the SrTiO₃ 2DEG measured using (a) *s*-, (b) *p*-polarised, and (c) the sum of *s*- and *p*-polarised 43 eV photons, and normalised to the same total intensity scaling. A schematic of the electronic orbitals that should be dominant for the respective experimental geometries and the resulting Fermi surfaces are also shown, in good agreement with our assignment of dominant orbital characters of the subbands in the main text.



Supplementary Figure 3: (a) Orbital character, and (b) $\langle S_x \rangle$, (c) $\langle S_y \rangle$ and (d) $\langle S_z \rangle$ components of the spin angular momentum for the entire calculated Fermi surface. (e) In-plane spin texture of outer (top) and inner (bottom) branches of successive Fermi surface sheets. The net winding direction is shown in the centre of each plot.



Supplementary Figure 4: Layer-projected calculations of the electronic structure of the SrTiO₃ 2DEG, integrated over (a) the full 30 unit cell (u.c.) supercell, and (b)–(g) individual or few unit cell regions, as labelled in the figure.